Cryo-electron tomography of Birbeck granules reveals the molecular mechanism of langerin lattice formation

Authors: Toshiyuki Oda[1*], Haruaki Yanagisawa[2], Hideyuki Shinmori [3], Youichi Ogawa[4], and Tatsuyoshi Kawamura[4]

Affiliations: [1] Department of Anatomy and Structural Biology, Graduate School of Medicine, University of Yamanashi, 1110 Shimokato, Chuo, Yamanashi, 409-3898, Japan. [2] Department of Cell Biology and Anatomy, Graduate School of Medicine, the University of Tokyo, 7-3-1 Hongo, Bunkyo-ku, Tokyo, 113-0033, Japan.

[3] Faculty of Life and Environmental Science, University of Yamanashi, 4-4-37 Takeda, Kofu, Yamanashi, 400-8510, Japan

[4] Department of Dermatology, Faculty of Medicine, University of Yamanashi, 1110 Shimokato, Chuo, Yamanashi, 409-3898, Japan.

*Correspondence to: toda@yamanashi.ac.jp

Abstract

Langerhans cells are specialized antigen-presenting cells localized within the epidermis and mucosal epithelium. Upon contact with Langerhans cells, pathogens are captured by the C-type lectin langerin and internalized into a structurally unique vesicle known as a Birbeck granule. Although the immunological role of Langerhans cells and Birbeck granules have been extensively studied, the mechanism by which the characteristic zippered membrane structure of Birbeck granules is formed remains elusive. In this study, we observed isolated Birbeck granules using cryo-electron tomography and reconstructed the 3D structure of the repeating unit of the honeycomb lattice of langerin at 6.4 Å resolution. We found that the interaction between the two langerin trimers was mediated by docking the flexible loop at residues 258-263 into the secondary carbohydrate-binding cleft. Mutations within the loop inhibited Birbeck granule formation and the internalization of HIV pseudovirus. These findings suggest a molecular mechanism for membrane zippering during Birbeck granule biogenesis and provide insight into the role of langerin in the defense against viral infection.

35 **Introduction**

36 The epidermis and mucosa provide the first line of defense against pathogens. In these tissues,
37 specialized antigen-presenting cells called Langerhans cells capture pathogens by
38 recognizing their surface mannose-containing oligosaccharides via the C-type lectin langerin
39 (Valladeau et al., 2003; Doebel et al., 2017). Pathogens internalized via langerin are enclosed
40 in a specialized organelle called a Birbeck granule, which has a central striated lamella
41 between closely apposed membranes (Birbeck et al., 1961; Valladeau et al., 2000;
42 McDermott et al., 2004; Valladeau et al., 1999). Once pathogens are captured, Langerhans
43 cells undergo maturation and migrate to peripheral lymph nodes, where they present
44 processed antigens to T cells (Merad et al., 2008; de_Jong MA, 2010; Rhodes et al., 2021).
45 Langerin is a type II transmembrane protein that is composed of a cytoplasmic tail, coiled-
46 coil neck region, and carbohydrate recognition domain (CRD) (Stambach and Taylor, 2003;
47 Valladeau et al., 1999; Valladeau et al., 2000) (Figure 1A). Through the coiled-coil neck
48 region, langerin forms a trimer, which is functionally important for oligosaccharide binding
49 (Stambach and Taylor, 2003; Weis and Drickamer, 1996; Weis and Drickamer, 1994). The
50 calcium-dependent carbohydrate-binding capacity of langerin CRD is essential for the
51 formation of Birbeck granules because the removal of calcium ions causes them to unzip and

52 disintegrate (Stambach and Taylor, 2003; Bartosik, 1992). It has been proposed that the "face-
53 to-face" interaction between the langerin trimers via CRDs confers the characteristic zippered
54 membranes with a central striation of Birbeck granules (Thepaut et al., 2009) (Figure 1B and
55 1C). However, the precise molecular mechanism of Birbeck granule formation is unknown
56 because of the lack of a high-resolution structure.

57 Langerin's high affinity for mannose and oligo-mannose allows Langerhans cells to capture
58 a wide range of pathogens, including *Saccharomyces cerevisiae, Candida albicans,*
59 *Mycobacterium leprae,* herpes simplex virus, and human immunodeficiency virus-1 (HIV-1)
60 (Tateno et al., 2010; Hunger et al., 2004; de Jong et al., 2010; de Witte et al., 2007; Turville et al.,
61 2002). Although Langerhans cells in the mucosa are the initial target of HIV-1 in sexually
62 transmitted infections, the efficiency of Langerhans cell infection is low, requiring high viral
63 loads of HIV-1 to infect cells (Kawamura et al., 2001; Kawamura et al., 2000; Ogawa et al., 2013).
64 The resistance of Langerhans cells to HIV-1 infection is mediated by the efficient internalization
65 of HIV-1 into Birbeck granules and subsequent autophagic degradation (de Witte et al., 2007;
66 Ribeiro et al., 2016). Therefore, elucidating the mechanism by which HIV-1 is internalized into
67 Birbeck granules is essential to understanding the role of Langerhans cells as a barrier to HIV-1
68 infection.

69 In the present study, we reconstructed the 3D structure of isolated Birbeck granules using cryo-
70 electron tomography and identified a flexible loop region that is crucial for Birbeck granule
71 formation and virus internalization.
72
73 **Results**
74 **Cryo-electron microscopy of isolated Birbeck granules**
75 Exogenous expression of langerin in mammalian cell lines readily reproduces the formation
76 of Birbeck granules (McDermott et al., 2004). We found that the addition of yeast mannan to
77 langerin-expressing cells enhances the formation of large Birbeck granules (Figure 1C). To
78 purify these Birbeck granules, we expressed SNAP-tagged human langerin in 293T cells,
79 biotinylated the tag by incubation with benzylguanine-biotin, and immunoprecipitated the
80 Birbeck granules using streptavidin agarose (Figure 1D and S1A). Under cryo-electron
81 microscopy, the isolated Birbeck granules were observed to be thin lamellar vesicles of
82 assorted sizes, similar to those reported previously (Figure 1E, 1F, and S1B) (Sagebiel and
83 Reed, 1968; Lenormand et al., 2013). Unlike regular 2D crystals of proteins, Birbeck
84 granules appear wavy, suggesting structural heterogeneity. The 2D classification of the
85 segmented images extracted from the micrographs showed nearly three-fold symmetrical

86 arrangements of pores with a diameter of approximately 10 nm; however, no clear crystalline
87 lattice was observed (Figure 1G). Although most Birbeck granules were oriented in
88 approximately the same direction with respect to the beam axis, some granules were twisted,
89 providing different views that were sufficient for 3D reconstruction (Figure S1C).
90

91 **Subtomogram averaging of the repeating unit of Birbeck granules**

92 We conducted cryo-electron tomography of the isolated Birbeck granules and reconstructed
93 the repeating units by averaging the subtomograms (Figure 2 and S2A). The initial density
94 map (Figure 2A) shows a langerin trimer (blue) with three inverted trimers (red) attached to
95 the CRDs. However, because of the flexibility between each langerin trimer, the resolution
96 was limited to ~24 Å. To improve the resolution, we generated a mask enclosing the central
97 langerin trimer and three attached CRDs and performed focused refinement and 3D
98 classification (Figure 2B). The resolution was improved to 6.4 Å (Figure S2B), which clearly
99 visualized the alpha helices and enabled us to generate a model based on the previously
100 reported crystal structure of the langerin trimer (Feinberg et al., 2010). We then performed a
101 two-body refinement to visualize the spatial relationship between the two opposing langerin
102 trimers (Nakane et al., 2018). Based on this refinement (Figure 2C), we built a honeycomb

103 lattice model (Figure 2D and Movie S1), which agrees with the striation of the Birbeck
104 granules observed by ultra-thin section electron microscopy and the ~10 nm pores visualized
105 in the 2D classification images (Figure 1C and 1G) (Birbeck et al., 1961). However, in reality,
106 the honeycomb lattice is non-uniform because of the structural heterogeneity.
107

108 **Interaction between the two langerin trimers via flexible loops**

109 An in-depth analysis of the interaction region between the two CRDs (Figure 3) revealed that
110 the interaction is mediated by a loop at residues 258-263, which is highly flexible in the
111 crystal structure (Feinberg et al., 2010). The interaction between the two CRDs appears to be
112 maintained by docking the loops of two langerin molecules into each other's lateral cleft,
113 which constitutes the secondary carbohydrate-binding site (Figure 3A, pink circles)
114 (Chatwell et al., 2008). The interaction between the two CRDs is flexible because the first
115 eigenvector of the multi-body analysis represents an approximately 30° tilting motion with
116 the loop as the fulcrum (Figure 3B, and Movie S2). Interestingly, loop 258-263 of the inverted
117 molecule appears to participate in the secondary carbohydrate-binding site of the upright
118 molecule (Figure 3A). A previous study found that the secondary calcium-independent
119 binding site has a lower affinity for carbohydrate ligands than the primary calcium-dependent

120 binding site (Chatwell et al., 2008). The docked loop 258-263 may provide additional
121 interactions with the hydroxyl group of mannose via Glu261 and Asp263, thus increasing the
122 affinity of the secondary binding site when two langerin trimers form a complex. Furthermore,
123 the Trp264Arg mutation is associated with a lack of Birbeck granules (Verdijk et al., 2005;
124 Figdor et al., 2002). Trp264 may also be involved in docking the loop into the cleft; however,
125 it is more likely that disruption of the hydrophobic core of the CRD is responsible for this
126 defect in Birbeck granule formation (Chatwell et al., 2008).
127

128 **Loop 258-263 is essential for Birbeck granule formation**

129 To investigate the importance of loop 258-263 in the biogenesis of Birbeck granules, we
130 mutated three residues in the loop: Met260Ala, Glu261Arg, and Asp263Lys, and generated
131 three mutated langerin constructs, each carrying one (MRGD), two (MRGK), or three
132 mutations (ARGK). We expressed these three langerin mutants in 293T cells and induced
133 Birbeck granule formation by adding yeast mannan (Figure 4A). Under ultra-thin section
134 microscopy, wild-type langerin produced Birbeck granules a few micrometers in length in
135 the presence of mannan (Figure 4A, MEGD WT). As the number of mutations increased, the
136 length of Birbeck granules decreased. With two point mutations (MRGK), some cross-

137 sections became spherical rather than rod-shaped, suggesting that the Birbeck granules failed
138 to extend. With three mutations (ARGK), clusters of Birbeck granules were not observed,
139 with isolated individual granules observed instead. The length of individual Birbeck granules
140 and the total length of granules per area were measured to confirm the above observations
141 (Figure 4B and 4C). In contrast, the number of the Birbeck granules showed less significant
142 differences because numerous short fragments were present in the mutant specimen (Figure
143 4D). These results demonstrate the importance of loop 258-263 in the biogenesis of Birbeck
144 granules.
145

146 **Loop 258-263 is crucial for the internalization of HIV pseudovirus**

147 To investigate the impact of the mutations in loop 258-263 on virus internalization by Birbeck
148 granules, we added lentiviruses pseudo-typed with the HIV-1 env protein to langerin-
149 expressing 293T cells. Ultra-thin section electron microscopy confirmed internalization of
150 viruses into Birbeck granules (Figure S3A). After 30 min of incubation, we retrieved viruses
151 attached to the surface langerin by washing with EDTA buffer, removed non-specifically
152 attached viruses by trypsinization, and isolated the Birbeck granules using streptavidin-
153 agarose (Figure 5). A langerin mutant that lost its calcium-binding capacity (Stambach and

154 Taylor, 2003) was used as the negative control (Figure 5, lectin (-)). The HIV pseudoviruses
155 attached to both wild-type and ARGK mutant langerin and the attachment was abolished by
156 the addition of mannan (Figure 5A). This indicated that the mutation of the loop did not
157 disrupt the binding of the glycosylated envelope proteins to the primary carbohydrate-
158 binding sites. In contrast, the internalization of the pseudovirus was significantly inhibited
159 by the ARGK mutation (Figure 5B and 5C). These results suggest that disruption of Birbeck
160 granule formation by the mutation of loop 258-263 inhibited the internalization of HIV
161 pseudovirus.
162

163 **Discussion**

164 **Virus internalization mechanism of Birbeck granules**

165 In the present study, we reconstructed the 3D structure of isolated Birbeck granules and found
166 that docking of the flexible loop 258-263 into the secondary carbohydrate-binding cleft is
167 essential for assembly of the langerin lattice. In agreement with this observation, we showed
168 that mutations introduced into the loop inhibited Birbeck granule formation and
169 internalization of HIV pseudovirus. Based on the structure of the glycosylated HIV env
170 protein (Stewart-Jones et al., 2016; Pan et al., 2020), we propose a model of HIV

171 internalization by langerin (Figure 6A and 6B). A previous study proposed that N-linked
172 high-mannose oligosaccharides bind to langerin at both primary and secondary carbohydrate-
173 binding sites (Chatwell et al., 2008). Our model requires bending of the coiled-coil necks of
174 the two langerin trimers to form a complex with HIV-1 env via the high-mannose
175 oligosaccharide (Figure 6B). Although the triple coiled-coil structure of the neck domain
176 does not seem to bend strongly, the coiled-coil prediction profile suggests that the N-terminal
177 part of the neck does not necessarily form a rigid triple coiled coil (Lupas et al., 1991) (Figure
178 S1D). Thus, we speculate that the neck region of the langerin trimer is flexible and swings
179 on the cell surface, allowing loop 258-263 of one trimer to dock into the cleft of an adjacent
180 trimer. Once the triad structure, consisting of two langerin trimers and one env protein, is
181 formed, the elasticity of the neck region can deform the cell membrane and initiate
182 invagination. The formation of clathrin pits may also be involved in membrane invagination,
183 because the cytoplasmic ends of Birbeck granules are coated with clathrin (Mc et al., 2002).
184 Additionally, it is possible that other intracellular mechanisms such as the actin cytoskeleton,
185 are involved in this membrane deformation process because annexin A2 is required for the
186 proper formation of Birbeck granules (Thornton et al., 2020).
187

188 **Significance of langerin-specific secondary carbohydrate-binding cleft**

189 It is noteworthy that the docking of loop 258-263 into the secondary calcium-independent
190 carbohydrate-binding cleft, which is not found in other C-type lectins (Chatwell et al., 2008),
191 mediates the assembly of the langerin lattice. In DC-SIGN, which is another C-type lectin
192 expressed in dendritic cells, and is closely related to langerin, the region corresponding to the
193 secondary carbohydrate-binding site of langerin forms a shallow pocket, that is occupied by
194 two calcium ions (Figure 7A) (Guo et al., 2004; Geijtenbeek et al., 2000; Geijtenbeek et al.,
195 2000). This structural difference between langerin and DC-SIGN may account for the
196 inability of DC-SIGN to form Birbeck granules despite its high sequence similarity to
197 langerin (Cambi et al., 2009). Another characteristic of the secondary carbohydrate-binding
198 site of langerin is its weak affinity for mannose and maltose (Chatwell et al., 2008). This may
199 reflect that the sugar-binding surface of langerin CRD is less negatively charged than that of
200 DC-SIGN CRD (Figure 7A) (Chatwell et al., 2008). Moreover, the interaction between the
201 secondary binding site and mannose/maltose is mainly mediated by backbone amide and
202 carbonyl groups (Chatwell et al., 2008). It is possible that the side chains of Glu261 and
203 Asp263 of loop 258-263 docked into the cleft of an adjacent langerin CRD provide the
204 negative charge required for stabilizing oligo-mannose bound to the secondary binding site

205 (Figure 7A and B). In agreement with this hypothesis, in the present study the Asp263Lys
206 mutation caused a significant defect in Birbeck granule formation. The secondary
207 carbohydrate-binding site may only be fully functional when two langerin trimers are bound
208 to each other (Figure 6 and 7B). The effect of the Met260Ala mutation on Birbeck granule
209 formation was unexpected, because the mutation was supposed to be silent in terms of side
210 chain charge. The observed structural variation of the langerin trimer complex suggests that
211 the side chain of Met260 acts as a hook to stabilize the interface between the two intersecting
212 loops.
213 Our model of Birbeck granule formation suggests that oligosaccharide ligands are captured
214 by the lateral surface of langerin (Figure 6). In contrast, DC-SIGN binds to dengue virus on
215 its upper surface (Pokidysheva et al., 2006). The difference in the ligand-binding manner
216 between langerin and DC-SIGN may contribute to their different carbohydrate recognition
217 preferences (Valverde et al., 2020; Takahara et al., 2004). Further studies are needed to
218 investigate the physiological significance of the unique carbohydrate-binding mechanism of
219 langerin and the honeycomb lattice structure of Birbeck granules.
220
221

222 **Methods**

223 ***Isolation of Birbeck granules***

224 The cDNA of human langerin was obtained from the Mammalian Gene Collection library
225 (Dnaform Inc., Yokohama, Japan) and was subcloned into pcDNA3.1-IRES-GFP (Schaefer
226 et al., 2008). A codon-optimized sequence coding SNAP-3×HA-HRV3C cleavage site
227 (obtained from ThermoFisher Scientific, Waltham, MA) was inserted immediately before the
228 start codon of the langerin sequence (Cole, 2013). O^6-benzylguanine-biotin was obtained by
229 reacting 16 mM O^6-benzylguanine-amine (Accela ChemBio, Shanghai, China) with 50 mM
230 biotin-AC_5-Osu (Dojindo, Kumamoto, Japan) and 30 mM triethylamine in
231 dimethylformamide for 24 hours at 30℃. Lenti-X 293T cells (TakaraBio, Tokyo, Japan) were
232 transfected with the langerin-expression plasmid by electroporation using ECM630
233 electroporator (BTX, Holliston, MA) and seeded onto the polyethylenimine-coated dish (PEI,
234 obtained from Fujifilm Wako Chemicals, Osaka, Japan). After 48-hour culturing in
235 DMEM+10% fetal bovine serum (FBS), the culture medium was replaced with serum-free
236 DMEM containing 10 μM O^6-benzylguanine-biotin and 10 μg/ml yeast mannan (Nacalai
237 tesque, Kyoto, Japan) and the cells were incubated for 30 min at 37 ℃. The cells were then
238 collected by scraping and washed five times with isotonic HMC buffer (Hepes 30 mM, pH

239 7.2, 150 mM NaCl, 2 mM $MgCl_2$, 2 mM $CaCl_2$, protease inhibitor cocktail (Nacalai tesque)).
240 The washed cells were homogenized with a Dounce glass homogenizer and were further
241 disrupted by sonication for 8 seconds using a Q125 sonicator (Qsonica, Newtown, CT). The
242 cell homogenate was loaded on top of a discontinuous Opti-prep density gradient (10-20-
243 40% layers, ThermoFisher Scientific) and ultracentrifuged for 1 hour at 100,000×g. The
244 fraction at the interface of 20/40% layers was collected and diluted 10-fold with HMC buffer
245 and was again disrupted by sonication for 2 min (120 cycles of 1-sec pulse and 3-sec wait)
246 at 4℃. Large debris was removed by filtration through a 20 μm-pore polyethylene mesh (GL
247 Science, Tokyo, Japan) and the cell lysate was incubated with a 30 μl slurry of streptavidin
248 agarose (Solulink, San Diego, CA) overnight at 4℃. The streptavidin agarose beads were
249 washed five times with HMC buffer and the bound Birbeck granules were eluted by overnight
250 digestion using home-made E. coli overexpressed His×6-HRV3C protease in HMC buffer at
251 4℃. After digestion and elution, HRV3C protease was removed by incubating the elute with
252 Ni-NTA resin (Qiagen, Düsseldorf, Germany). About 50 μl of elute containing released
253 Birbeck granules (approximately 0.05 mg/ml) were obtained from twelve 100-mm dishes of
254 cell culture.
255

256 ***Cryo-electron microscopy of isolated Birbeck granules***

257 5 µl of the purified Birbeck granules was applied onto freshly glow-discharged holey carbon
258 grids, Quantifoil R1.2/1.3 Cu/Rh 200 mesh (Quantifoil Micro Tools GmbH, Großlöbichau,
259 Germany), blotted from the backside to concentrate the granules by filtration through the
260 holes, and 4 µl of HMC buffer containing cytochrome *c*-stabilized 15-nm colloidal gold (BBI
261 Solutions) was applied for attachment of fiducial markers (Oda et al., 2015). Grids were
262 blotted from the backside for 10 seconds at 4°C under 99% humidity and plunge frozen in
263 liquid ethane using Vitrobot Mark IV (Thermo Fisher Scientific). We removed one of the
264 blotting arms for one-side blotting because Birbeck granules would be absorbed onto the
265 filter paper. Images were recorded using a Titan Krios G3i microscope at the University of
266 Tokyo (Thermo Fisher Scientific) at 300 keV, a Gatan Quantum-LS Energy Filter (Gatan,
267 Pleasanton, CA) with a slit width of 20 eV, and a Gatan K3 Summit direct electron detector
268 in the electron counting mode. The nominal magnification was set to 33,000× with a physical
269 pixel size of 2.67 Å/pixel. Movies were acquired using the SerialEM software (Mastronarde,
270 2005), and the target defocus was set to 3-6 µm. The angular range of the tilt series was from
271 -60° to 60° with 3.0° increments. Each movie was recorded for 0.74 sec with a total dose of
272 1.24 electrons/$Å^2$ and subdivided into 20 frames. The total dose for one tilt series acquisition

273 is thus 50 electrons/Å^2.

274

275 ***Data processing***

276 Movies were subjected to beam-induced motion correction using MotionCor2 (Zheng et al.,
277 2017), and tilt series images were aligned, CTF corrected, and back-projected to reconstruct
278 3D tomograms using the IMOD software package (Kremer et al., 1996). For the subsequent
279 analysis using Relion-4.0 (Kimanius et al., 2021), the tomogram positioning step was skipped
280 to keep the angle offset and the Z-shift zero. Tomograms were 4×binned to reduce loads of
281 the calculation. The areas of the Birbeck granules were manually selected using the 3dmod
282 model tool (Kremer et al., 1996), and the center coordinates for the subtomograms were
283 determined by placing points at 8-pixel (~8.5 nm) intervals within the selected area using a
284 custom-made Ruby script (Metlagel et al., 2007). For twisting Birbeck granules (Figure S1C),
285 center points were picked manually by selecting the mid-portion of the lamella. Volumes with
286 32×32×32 pixel-dimensions were extracted from 8×binned tomograms and were averaged
287 using the PEET software suite (Nicastro et al., 2006). A randomly selected subtomogram was
288 used for the initial reference. Alignments were repeated five times for 8×binned and twice
289 for 4×binned tomograms with 64×64×64 pixel-dimensions. The coordinates and the rotation

290 angles of the aligned subtomograms were exported to Relion-4.0. Initial
291 pseudosubtomograms were generated with the box size of 128 pixels, the cropped box size
292 of 64 pixels, and the binning factor of 4. The subtomograms were 3D refined using a spherical
293 mask of 320-Å diameter. After 3D classification, 2×binned pseudosubtomograms were
294 generated with the box size of 256 pixels and the cropped box size of 128 pixels based on the
295 refined coordinates and angles and were 3D refined using the same spherical mask. Finally,
296 un-binned pseudosubtomograms were generated with a box size of 256 pixels and a cropped
297 box size of 128 pixels. 3D refinement was done using a tighter mask enclosing the central
298 upright langerin molecule and three bound CRDs, and low-resolution subtomograms were
299 removed by 3D classification. The alignment was further refined using CTF refinement and
300 frame alignment. We initially refined the surrounding inverted langerin molecule by 3D
301 refinement masking out the central upright molecule, but the refinement was biased toward
302 the center. To improve the map quality of the inverted molecule, we applied 3D multi-body
303 refinement (Nakane et al., 2018), which successfully compensated for the flexibility between
304 the upright and the inverted molecules. For model building, the crystal structure of langerin
305 trimer (Feinberg et al., 2010) (PDB ID: 3KQG) was fitted into the map using UCSF Chimera
306 (Pettersen et al., 2004). Then, the fitted model was further refined using PHENIX real-space

307 refinement tool, and the refined model was validated using the comprehensive validation tool
308 (Adams et al., 2010). The Coulombic surfaces rendering was conducted using UCSF
309 Chimera and other model presentations, surface rendering, and morph movie generation were
310 conducted using ChimeraX (Goddard et al., 2018). The data processing and the statistics of
311 the model validation are summarized in Figure S2A and Table S1.
312

313 ***Ultrathin section electron microscopy of Birbeck granules***

314 Pellets of 293T cells with mannan-induced Birbeck granules were fixed with 4%
315 paraformaldehyde for 1 hour at 4℃ and stained with 1% osmium tetroxide and subsequently
316 with 1% uranium acetate. After dehydration in ethanol and acetone, the samples were
317 embedded in Quetol 812 resin (Nissin EM, Tokyo, Japan). 60-nm ultrathin sections were cut
318 using a ULTRACUT microtome (Reichert Leica) and mounted onto Formvar-coated copper
319 grid. Images were recorded using a JEM-2100F microscope (JEOL, Tokyo, Japan) at
320 University of Yamanashi operated at 200 keV equipped with an F216 CMOS camera (TVIPS
321 GmbH, Gauting, Germany). Length of Birbeck granules were measured using Fiji software
322 (Schindelin et al., 2012), and plots were generated using PlotsOfData web tool (Postma and
323 Goedhart, 2019). For total length of Birbeck granules per 100 μm^2, cross sections of cells

324 with nuclei of > 5 μm in diameter were selected, and the sum of the lengths of Birbeck
325 granules within the cells were measured. The areas of the cross sections were also measured
326 using Fiji software. 100 μm^2 corresponds to the approximate mean of the cross-sectional area
327 of one cell.
328
329 ***Lentivirus preparation***
330 Lentiviruses pseudotyped with HIV-1 env were prepared by transfecting the Lenti-X 293T
331 cells with pCMV-dR8.3 Δvpr (Addgene plasmid #8455), pLOX-CW-tdTomato, and pCEP4-
332 AD8gp160 (Adgene plasmid #123260) (Stewart et al., 2003; Heredia et al., 2019). The vector
333 pLOX-CW-tdTomato was generated by replacing the GFP sequence of pLOX-CWgfp
334 (Addgene plasmid #12241) (Salmon et al., 2000) with the tdTomato sequence derived from
335 pCDH-EF1-Luc2-P2A-tdTomato, a gift from Kazuhiro Oka (Addgene plasmid # 72486). The
336 transfections were carried out using the PEI-method with the ratio at PEI: dR8.3: tdTomato:
337 gp160 = 4:1:1:1. 16 hours post-transfection, the cells were washed three times with PBS and
338 incubated in a fresh medium for another 32 hours. The virus-containing medium was
339 collected and removed cell debris by a 1,000×g centrifuge and a 0.45 μm filtration (Millipore).
340 The obtained supernatants were immediately used for subsequent assays.

341

342 ***Virus attachment and internalization assay***

343 293T cells were transfected with wild type langerin, the ARGK mutant, and, as a negative
344 control, a lectin (-) mutant lacking calcium-binding ability. The lectin (-) langerin mutant was
345 generated by introducing three point-mutations at the calcium-binding site: Glu285Lys;
346 Asn287Lys; and Glu293Lys (Chatwell et al., 2008). We conducted surface labeling of
347 langerin-expressing cells and confirmed that these mutations did not alter the surface
348 expression of langerin (Figure S3B). 48 hours post-transfection, the cells were pre-treated
349 with or without 10 μg/ml yeast mannan for 5 min at 37℃. The cells were then incubated in
350 the pseudovirus-containing supernatants plus 10 μM O^6-benzylguanine-biotin and 10 μg/ml
351 DEAE-dextran (Sigma Aldrich, St. Louis, MO) with or without 10 μg/ml yeast mannan for
352 30 min at 37℃. After the incubation, supernatant containing unbound viruses were collected.
353 The cells were then washed with TBS-Ca buffer (20 mM Tris-HCl pH 7.4, 150 mM NaCl, 5
354 mM $CaCl_2$) three times, and the viruses attached to langerin at the cell surface was retrieved
355 by washing with TBS-EDTA buffer (20 mM Tris-HCl pH 7.4, 150 mM NaCl, 10 mM EDTA).
356 The collected supernatant of the medium and the TBS-EDTA buffer were centrifuged at
357 1,000×g for 5 min to remove cell debris, and the viruses were sedimented by ultra-

358 centrifugation at 100,000×g for 3 hours. After the TBS-EDTA washing, non-specifically
359 bound viruses were removed by trypsinization using 0.25 % (w/v) trypsin and 1mM EDTA
360 for 5 min at 37℃ as previously described (Burkard et al., 2014). Detached cells were washed
361 twice with DMEM+10 % FBS, and five times with TBS-Ca. Internalized viruses within
362 Birbeck granules were isolated from the washed cells by streptavidin-agarose precipitation
363 as described above. Viruses, langerin, and tubulin were detected by immunoblotting using
364 HIV-1 gag p24 antibody (1:1000 dilution, MAB7360, mouse monoclonal, R&D systems,
365 Minneapolis, MN), human CD207 antibody (1:1000 dilution, 11841-1-AP, rabbit polyclonal,
366 Proteintech Group Inc., Rosemont, IL), and tubulin antibody (1:3000 dilution, B-512, mouse
367 monoclonal, Sigma-Aldrich), respectively. ELSA was carried out using HIV Type 1 p24
368 Antigen ELISA kit (ZeptoMatrix, Buffalo, NY). The p24 antibody detected unprocessed
369 ($Pr55^{gag}$) and fully processed (p24) capsid proteins (Gonelli et al., 2019). Band intensities
370 were measured using ImageJ (Schneider et al., 2012). Surface labeling was carried out by
371 treating the cells with 0.5mM biotin-sulfo-osu (Dojindo, Osaka, Japan) for 30 min at 37℃.
372 Cells were washed three times with TBS and collected by scraping. Surface-expressed
373 proteins were extracted by incubating the cells in TBS plus 1% Triton X-100 for 1 hour at
374 4℃, and immunoprecipitated using streptavidin agarose. ELISA using p24 antibody showed

375 that >99% of the viruses remained in the supernatant (Figure S3C).

376

377 ***Isolation of langerin-expressing stable cell lines***

378 We isolated a cell line stably expressing langerin by selecting HEK293 cells using G418

379 (Sigma Aldrich). However, the expression levels of the isolated cell line was 10~20% of that

380 of the transiently expressing cells (Figure S3D). These cells can form Birbeck granules in the

381 presence of yeast mannan, but with lower efficiency (Figure S3E and F). Therefore, we chose

382 to use the transient expression system in the main experiments.

383

384

385 **Author contributions**

386 T.O. conceived the project and designed the experiments. T.O., H.Y., and H.S. performed the
387 experiments. T.O., and H.Y. analyzed the data. T.O., H.Y., Y.O., and T.K. wrote the
388 manuscript.

389

390 **Data availability**

391 The map and the model will be available on the EMDB upon publication under the following
392 accession numbers: EMD-32906, and PDB 7WZ8.

393

394 **Acknowledgements**

395 We thank Mrs. Natsuko Maruyama (University of Yamanashi) for technical assistance. This
396 research is partially supported by Platform Project for Supporting Drug Discovery and Life
397 Science Research (Basis for Supporting Innovative Drug Discovery and Life Science
398 Research (BINDS)) from Japan Agency for Medical Research and Development (AMED)
399 under Grant Number JP19am0101115. This research was conducted using the Fujitsu
400 PRIMERGY CX400M1/CX2550M5 (Oakbridge-CX) and the SGI Rackable C2112-
401 4GP3/C1102-GP8 (Reedbush-H/L) in the Information Technology Center, The University of

402 Tokyo. This work was supported by the Takeda Science Foundation (to T.O.), the Daiichi
403 Sankyo Foundation of Life Science (to T.O.), the Japan Society for the Promotion of Science
404 (KAKENHI Grant number JP21H02654 to T.O.), and the Naito Foundation (to T.O.).
405 Molecular graphics and analyses performed with UCSF ChimeraX, developed by the
406 Resource for Biocomputing, Visualization, and Informatics at the University of California,
407 San Francisco, with support from National Institutes of Health R01-GM129325 and the
408 Office of Cyber Infrastructure and Computational Biology, National Institute of Allergy and
409 Infectious Diseases.

410

411

412 **References**

413

414 Adams, P.D., Afonine, P.V., Bunkoczi, G., Chen, V.B., Davis, I.W., Echols, N., Headd,
415 J.J., Hung, L.W., Kapral, G.J., Grosse-Kunstleve, R.W. et al. 2010. PHENIX: a
416 comprehensive Python-based system for macromolecular structure solution. *Acta.*
417 *Crystallogr. D. Biol. Crystallogr.* **66**, 213-221.
418 Bartosik, J. 1992. Cytomembrane-derived Birbeck granules transport horseradish
419 peroxidase to the endosomal compartment in the human Langerhans cells. *J. Invest.*
420 *Dermatol.* **99**, 53-58.
421 Birbeck, M.S., Breathnach, A.S., and Everall, J.D. 1961. An electron microscope study of
422 basal melanocytes and high-level clear cells (Langerhans cells) in vitiligo. *J. Invest.*
423 *Dermatol.* **37**, 51-63.
424 Burkard, C., Bloyet, L.M., Wicht, O., van, Kuppeveld F.J., Rottier, P.J., de, Haan C.A., and
425 Bosch, B.J. 2014. Dissecting virus entry: replication-independent analysis of virus binding,
426 internalization, and penetration using minimal complementation of beta-galactosidase.
427 *PLoS. One.* **9**, e101762.
428 Cambi, A., Beeren, I., Joosten, B., Fransen, J.A., and Figdor, C.G. 2009. The C-type lectin
429 DC-SIGN internalizes soluble antigens and HIV-1 virions via a clathrin-dependent
430 mechanism. *Eur. J. Immunol.* **39**, 1923-1928.
431 Chatwell, L., Holla, A., Kaufer, B.B., and Skerra, A. 2008. The carbohydrate recognition
432 domain of Langerin reveals high structural similarity with the one of DC-SIGN but an
433 additional, calcium-independent sugar-binding site. *Mol. Immunol.* **45**, 1981-1994.
434 Cole, N.B. 2013. Site-specific protein labeling with SNAP-tags. *Curr. Protoc. Protein. Sci.*
435 **73**, 30.1.1-30.1.16.
436 de Jong, M.A., de, Witte L., Taylor, M.E., and Geijtenbeek, T.B. 2010. Herpes simplex
437 virus type 2 enhances HIV-1 susceptibility by affecting Langerhans cell function. *J.*
438 *Immunol.* **185**, 1633-1641.
439 de_Jong MA, Geijtenbeek T.B. 2010. Langerhans cells in innate defense against pathogens.
440 *Trends. Immunol.* **31**, 452-459.
441 de Witte, L., Nabatov, A., Pion, M., Fluitsma, D., de Jong M.A., de, Gruijl T., Piguet, V.,
442 van, Kooyk Y., and Geijtenbeek, T.B. 2007. Langerin is a natural barrier to HIV-1

443 transmission by Langerhans cells. *Nat. Med.* **13**, 367-371.
444 Doebel, T., Voisin, B., and Nagao, K. 2017. Langerhans Cells - The Macrophage in
445 Dendritic Cell Clothing. *Trends. Immunol.* **38**, 817-828.
446 Feinberg, H., Powlesland, A.S., Taylor, M.E., and Weis, W.I. 2010. Trimeric structure of
447 langerin. *J. Biol. Chem.* **285**, 13285-13293.
448 Figdor, C.G., van, Kooyk Y., and Adema, G.J. 2002. C-type lectin receptors on dendritic
449 cells and Langerhans cells. *Nat. Rev. Immunol.* **2**, 77-84.
450 Geijtenbeek, T.B., Kwon, D.S., Torensma, R., van, Vliet S.J., van, Duijnhoven G.C.,
451 Middel, J., Cornelissen, I.L., Nottet, H.S., KewalRamani, V.N., Littman, D.R. et al. 2000.
452 DC-SIGN, a dendritic cell-specific HIV-1-binding protein that enhances trans-infection of
453 T cells. *Cell.* **100**, 587-597.
454 Geijtenbeek, T.B., Krooshoop, D.J., Bleijs, D.A., van, Vliet S.J., van, Duijnhoven G.C.,
455 Grabovsky, V., Alon, R., Figdor, C.G., and van, Kooyk Y. 2000. DC-SIGN-ICAM-2
456 interaction mediates dendritic cell trafficking. *Nat. Immunol.* **1**, 353-357.
457 Goddard, T.D., Huang, C.C., Meng, E.C., Pettersen, E.F., Couch, G.S., Morris, J.H., and
458 Ferrin, T.E. 2018. UCSF ChimeraX: Meeting modern challenges in visualization and
459 analysis. *Protein. Sci.* **27**, 14-25.
460 Gonelli, C.A., Khoury, G., Center, R.J., and Purcell, D.F.J. 2019. HIV-1-based Virus-like
461 Particles that Morphologically Resemble Mature, Infectious HIV-1 Virions. *Viruses.* **11**,
462 507.
463 Guo, Y., Feinberg, H., Conroy, E., Mitchell, D.A., Alvarez, R., Blixt, O., Taylor, M.E.,
464 Weis, W.I., and Drickamer, K. 2004. Structural basis for distinct ligand-binding and
465 targeting properties of the receptors DC-SIGN and DC-SIGNR. *Nat. Struct. Mol. Biol.* **11**,
466 591-598.
467 Heredia, J.D., Park, J., Choi, H., Gill, K.S., and Procko, E. 2019. Conformational
468 Engineering of HIV-1 Env Based on Mutational Tolerance in the CD4 and PG16 Bound
469 States. *J. Virol.* **93**, e00219-00219.
470 Hunger, R.E., Sieling, P.A., Ochoa, M.T., Sugaya, M., Burdick, A.E., Rea, T.H., Brennan,
471 P.J., Belisle, J.T., Blauvelt, A., Porcelli, S.A. et al. 2004. Langerhans cells utilize CD1a and
472 langerin to efficiently present nonpeptide antigens to T cells. *J. Clin. Invest.* **113**, 701-708.
473 Kawamura, T., Cohen, S.S., Borris, D.L., Aquilino, E.A., Glushakova, S., Margolis, L.B.,
474 Orenstein, J.M., Offord, R.E., Neurath, A.R., and Blauvelt, A. 2000. Candidate
475 microbicides block HIV-1 infection of human immature Langerhans cells within epithelial

476 tissue explants. *J. Exp. Med.* **192**, 1491-1500.
477 Kawamura, T., Qualbani, M., Thomas, E.K., Orenstein, J.M., and Blauvelt, A. 2001. Low
478 levels of productive HIV infection in Langerhans cell-like dendritic cells differentiated in
479 the presence of TGF-beta1 and increased viral replication with CD40 ligand-induced
480 maturation. *Eur. J. Immunol.* **31**, 360-368.
481 Kimanius, D., Dong, L., Sharov, G., Nakane, T., and Scheres, S.H.W. 2021. New tools for
482 automated cryo-EM single-particle analysis in RELION-4.0. *Biochem. J.* **478**, 4169-4185.
483 Kremer, J.R., Mastronarde, D.N., and McIntosh, J.R. 1996. Computer visualization of
484 three-dimensional image data using IMOD. *J. Struct. Biol.* **116**, 71-76.
485 Lenormand, C., Spiegelhalter, C., Cinquin, B., Bardin, S., Bausinger, H., Angenieux, C.,
486 Eckly, A., Proamer, F., Wall, D., Lich, B. et al. 2013. Birbeck granule-like "organized
487 smooth endoplasmic reticulum" resulting from the expression of a cytoplasmic YFP-tagged
488 langerin. *PLoS. One.* **8**, e60813.
489 Lupas, A., Van, Dyke M., and Stock, J. 1991. Predicting coiled coils from protein
490 sequences. *Science.* **252**, 1162-1164.
491 Mastronarde, D.N. 2005. Automated electron microscope tomography using robust
492 prediction of specimen movements. *J. Struct. Biol.* **152**, 36-51.
493 Mc, Dermott R., Ziylan, U., Spehner, D., Bausinger, H., Lipsker, D., Mommaas, M.,
494 Cazenave, J.P., Raposo, G., Goud, B., de, la Salle H. et al. 2002. Birbeck granules are
495 subdomains of endosomal recycling compartment in human epidermal Langerhans cells,
496 which form where Langerin accumulates. *Mol. Biol. Cell.* **13**, 317-335.
497 McDermott, R., Bausinger, H., Fricker, D., Spehner, D., Proamer, F., Lipsker, D.,
498 Cazenave, J.P., Goud, B., De, La Salle H., Salamero, J. et al. 2004. Reproduction of
499 Langerin/CD207 traffic and Birbeck granule formation in a human cell line model. *J.*
500 *Invest. Dermatol.* **123**, 72-77.
501 Merad, M., Ginhoux, F., and Collin, M. 2008. Origin, homeostasis and function of
502 Langerhans cells and other langerin-expressing dendritic cells. *Nat. Rev. Immunol.* **8**, 935-
503 947.
504 Metlagel, Z., Kikkawa, Y.S., and Kikkawa, M. 2007. Ruby-Helix: an implementation of
505 helical image processing based on object-oriented scripting language. *J. Struct. Biol.* **157**,
506 95-105.
507 Nakane, T., Kimanius, D., Lindahl, E., and Scheres, S.H. 2018. Characterization of
508 molecular motions in cryo-EM single-particle data by multi-body refinement in RELION.

509 *Elife.* **7**, e36861.
510 Nicastro, D., Schwartz, C., Pierson, J., Gaudette, R., Porter, M.E., and McIntosh, J.R. 2006.
511 The molecular architecture of axonemes revealed by cryoelectron tomography. *Science.*
512 **313**, 944-948.
513 Oda, T., Yanagisawa, H., and Kikkawa, M. 2015. Detailed structural and biochemical
514 characterization of the nexin-dynein regulatory complex. *Mol. Biol. Cell.* **26**, 294-304.
515 Ogawa, Y., Kawamura, T., Matsuzawa, T., Aoki, R., Gee, P., Yamashita, A., Moriishi, K.,
516 Yamasaki, K., Koyanagi, Y., Blauvelt, A. et al. 2013. Antimicrobial peptide LL-37
517 produced by HSV-2-infected keratinocytes enhances HIV infection of Langerhans cells.
518 *Cell. Host. Microbe.* **13**, 77-86.
519 Pan, J., Peng, H., Chen, B., and Harrison, S.C. 2020. Cryo-EM Structure of Full-length
520 HIV-1 Env Bound With the Fab of Antibody PG16. *J. Mol. Biol.* **432**, 1158-1168.
521 Pettersen, E.F., Goddard, T.D., Huang, C.C., Couch, G.S., Greenblatt, D.M., Meng, E.C.,
522 and Ferrin, T.E. 2004. UCSF Chimera--a visualization system for exploratory research and
523 analysis. *J. Comput. Chem.* **25**, 1605-1612.
524 Pokidysheva, E., Zhang, Y., Battisti, A.J., Bator-Kelly, C.M., Chipman, P.R., Xiao, C.,
525 Gregorio, G.G., Hendrickson, W.A., Kuhn, R.J., and Rossmann, M.G. 2006. Cryo-EM
526 reconstruction of dengue virus in complex with the carbohydrate recognition domain of
527 DC-SIGN. *Cell.* **124**, 485-493.
528 Postma, M., and Goedhart, J. 2019. PlotsOfData-A web app for visualizing data together
529 with their summaries. *PLoS. Biol.* **17**, e3000202.
530 Rhodes, J.W., Botting, R.A., Bertram, K.M., Vine, E.E., Rana, H., Baharlou, H., Vegh, P.,
531 O'Neil, T.R., Ashhurst, A.S., Fletcher, J. et al. 2021. Human anogenital monocyte-derived
532 dendritic cells and langerin+cDC2 are major HIV target cells. *Nat. Commun.* **12**, 2147.
533 Ribeiro, C.M., Sarrami-Forooshani, R., Setiawan, L.C., Zijlstra-Willems, E.M., van,
534 Hamme J.L., Tigchelaar, W., van, der Wel N.N., Kootstra, N.A., Gringhuis, S.I., and
535 Geijtenbeek, T.B. 2016. Receptor usage dictates HIV-1 restriction by human TRIM5alpha
536 in dendritic cell subsets. *Nature.* **540**, 448-452.
537 Sagebiel, R.W., and Reed, T.H. 1968. Serial reconstruction of the characteristic granule of
538 the Langerhans cell. *J. Cell. Biol.* **36**, 595-602.
539 Salmon, P., Oberholzer, J., Occhiodoro, T., Morel, P., Lou, J., and Trono, D. 2000.
540 Reversible immortalization of human primary cells by lentivector-mediated transfer of
541 specific genes. *Mol. Ther.* **2**, 404-414.

542 Schaefer, M.R., Williams, M., Kulpa, D.A., Blakely, P.K., Yaffee, A.Q., and Collins, K.L.
543 2008. A novel trafficking signal within the HLA-C cytoplasmic tail allows regulated
544 expression upon differentiation of macrophages. *J. Immunol.* **180**, 7804-7817.
545 Schindelin, J., Arganda-Carreras, I., Frise, E., Kaynig, V., Longair, M., Pietzsch, T.,
546 Preibisch, S., Rueden, C., Saalfeld, S., Schmid, B. et al. 2012. Fiji: an open-source platform
547 for biological-image analysis. *Nat. Methods.* **9**, 676-682.
548 Schneider, C.A., Rasband, W.S., and Eliceiri, K.W. 2012. NIH Image to ImageJ: 25 years
549 of image analysis. *Nat. Methods.* **9**, 671-675.
550 Stambach, N.S., and Taylor, M.E. 2003. Characterization of carbohydrate recognition by
551 langerin, a C-type lectin of Langerhans cells. *Glycobiology.* **13**, 401-410.
552 Stewart, S.A., Dykxhoorn, D.M., Palliser, D., Mizuno, H., Yu, E.Y., An, D.S., Sabatini,
553 D.M., Chen, I.S., Hahn, W.C., Sharp, P.A. et al. 2003. Lentivirus-delivered stable gene
554 silencing by RNAi in primary cells. *RNA.* **9**, 493-501.
555 Stewart-Jones, G.B., Soto, C., Lemmin, T., Chuang, G.Y., Druz, A., Kong, R., Thomas,
556 P.V., Wagh, K., Zhou, T., Behrens, A.J. et al. 2016. Trimeric HIV-1-Env Structures Define
557 Glycan Shields from Clades A, B, and G. *Cell.* **165**, 813-826.
558 Takahara, K., Yashima, Y., Omatsu, Y., Yoshida, H., Kimura, Y., Kang, Y.S., Steinman,
559 R.M., Park, C.G., and Inaba, K. 2004. Functional comparison of the mouse DC-SIGN,
560 SIGNR1, SIGNR3 and Langerin, C-type lectins. *Int. Immunol.* **16**, 819-829.
561 Tateno, H., Ohnishi, K., Yabe, R., Hayatsu, N., Sato, T., Takeya, M., Narimatsu, H., and
562 Hirabayashi, J. 2010. Dual specificity of Langerin to sulfated and mannosylated glycans via
563 a single C-type carbohydrate recognition domain. *J. Biol. Chem.* **285**, 6390-6400.
564 Thepaut, M., Valladeau, J., Nurisso, A., Kahn, R., Arnou, B., Vives, C., Saeland, S., Ebel,
565 C., Monnier, C., Dezutter-Dambuyant, C. et al. 2009. Structural studies of langerin and
566 Birbeck granule: a macromolecular organization model. *Biochemistry.* **48**, 2684-2698.
567 Thornton, S.M., Samararatne, V.D., Skeate, J.G., Buser, C., Luhen, K.P., Taylor, J.R., Da,
568 Silva D.M., and Kast, W.M. 2020. The Essential Role of anxA2 in Langerhans Cell
569 Birbeck Granules Formation. *Cells.* **9**, 974.
570 Turville, S.G., Cameron, P.U., Handley, A., Lin, G., Pohlmann, S., Doms, R.W., and
571 Cunningham, A.L. 2002. Diversity of receptors binding HIV on dendritic cell subsets. *Nat.*
572 *Immunol.* **3**, 975-983.
573 Valladeau, J., Duvert-Frances, V., Pin, J.J., Dezutter-Dambuyant, C., Vincent, C.,
574 Massacrier, C., Vincent, J., Yoneda, K., Banchereau, J., Caux, C. et al. 1999. The

575 monoclonal antibody DCGM4 recognizes Langerin, a protein specific of Langerhans cells,
576 and is rapidly internalized from the cell surface. *Eur. J. Immunol.* **29**, 2695-2704.
577 Valladeau, J., Ravel, O., Dezutter-Dambuyant, C., Moore, K., Kleijmeer, M., Liu, Y.,
578 Duvert-Frances, V., Vincent, C., Schmitt, D., Davoust, J. et al. 2000. Langerin, a novel C-
579 type lectin specific to Langerhans cells, is an endocytic receptor that induces the formation
580 of Birbeck granules. *Immunity.* **12**, 71-81.
581 Valladeau, J., Dezutter-Dambuyant, C., and Saeland, S. 2003. Langerin/CD207 sheds light
582 on formation of birbeck granules and their possible function in Langerhans cells. *Immunol.*
583 *Res.* **28**, 93-107.
584 Valverde, P., Martinez, J.D., Canada, F.J., Arda, A., and Jimenez-Barbero, J. 2020.
585 Molecular Recognition in C-Type Lectins: The Cases of DC-SIGN, Langerin, MGL, and L-
586 Sectin. *Chembiochem.* **21**, 2999-3025.
587 Verdijk, P., Dijkman, R., Plasmeijer, E.I., Mulder, A.A., Zoutman, W.H., Mieke,
588 Mommaas A., and Tensen, C.P. 2005. A lack of Birbeck granules in Langerhans cells is
589 associated with a naturally occurring point mutation in the human Langerin gene. *J. Invest.*
590 *Dermatol.* **124**, 714-717.
591 Weis, W.I., and Drickamer, K. 1994. Trimeric structure of a C-type mannose-binding
592 protein. *Structure.* **2**, 1227-1240.
593 Weis, W.I., and Drickamer, K. 1996. Structural basis of lectin-carbohydrate recognition.
594 *Annu. Rev. Biochem.* **65**, 441-473.
595 Zheng, S.Q., Palovcak, E., Armache, J.P., Verba, K.A., Cheng, Y., and Agard, D.A. 2017.
596 MotionCor2: anisotropic correction of beam-induced motion for improved cryo-electron
597 microscopy. *Nat. Methods.* **14**, 331-332.
598

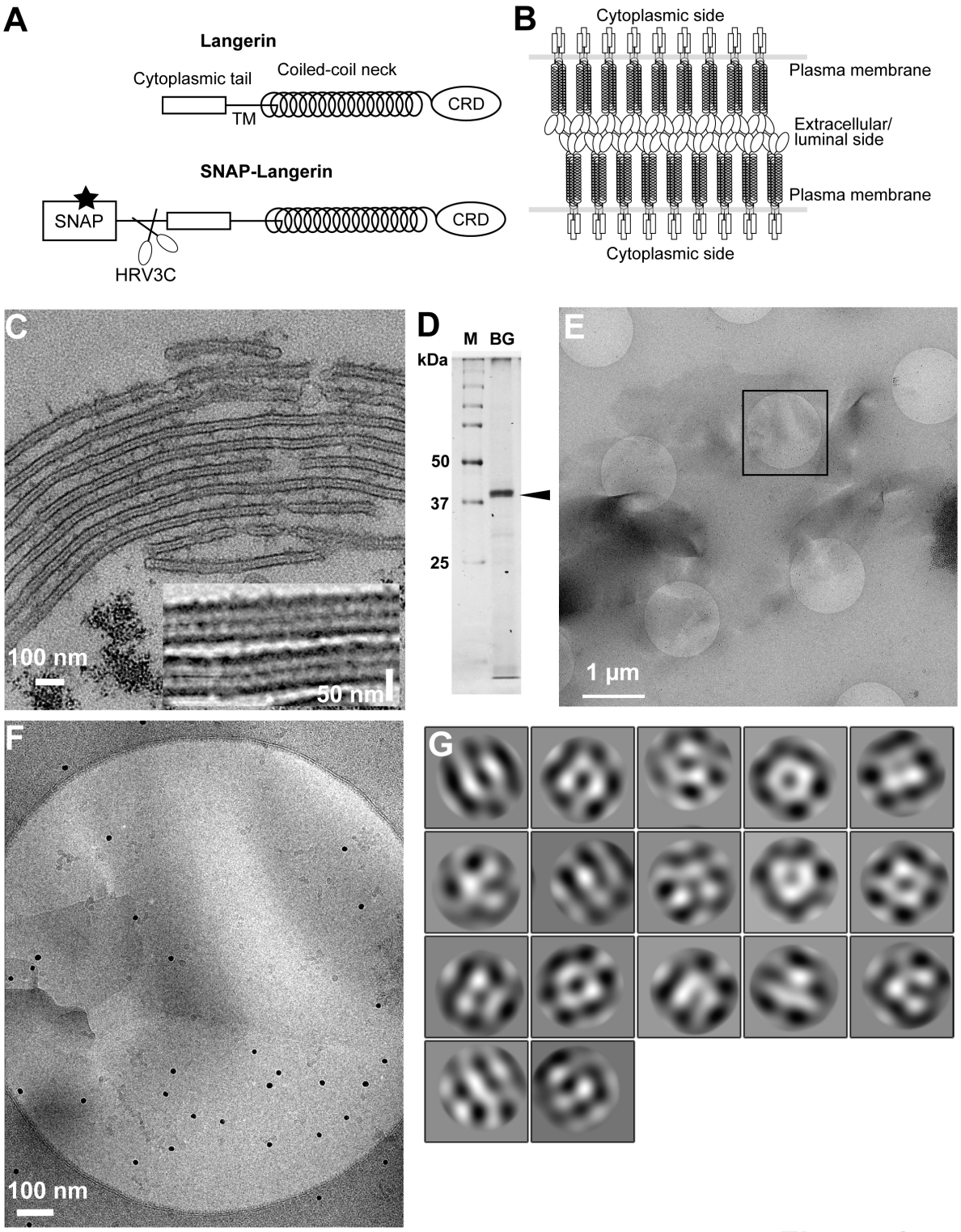
A
Langerin
Cytoplasmic tail
Coiled-coil neck
TM
CRD
SNAP-Langerin
SNAP
CRD
HRV3C
B
Cytoplasmic side
Plasma membrane
Extracellular/
luminal side
Plasma membrane
Cytoplasmic side
C
100 nm
50 nm
D
M
BG
kDa
50
37
25
E
1 µm
F
100 nm
G

Figure 1

599

600 **Figure 1: Isolation of Birbeck granules.** (A) Domain organization of langerin. Human
601 langerin is a 328-amino acids protein composed of an N-terminal cytoplasmic tail, a
602 transmembrane domain (TM), a coiled-coil neck, and a C-terminal carbohydrate-recognition
603 domain (CRD). We fused a SNAP-tag at the N-terminus of langerin and inserted an HRV3C
604 protease cleavage site between the tag and the langerin sequences. For streptavidin-mediated
605 precipitation of Birbeck granules, the SNAP-tag was biotinylated (star). (B) Model of
606 langerin oligomerization within Birbeck granules. Langerin trimers bind to each other face-
607 to-face via the CRDs, bringing the two layers of the plasma membrane closer together. (C)
608 Birbeck granules formed in 293T cells overexpressing langerin. Addition of yeast mannan
609 induced the formation of Birbeck granules a few micrometers long. Inset shows a magnified
610 view of Birbeck granules. (D) SDS-PAGE of isolated Birbeck granules. Purified langerin
611 (arrowhead) was released from streptavidin-agarose by HRV3C digestion. M: molecular
612 weight marker; and BG: isolated Birbeck granules. (E) Cryo-electron microscopy of isolated
613 Birbeck granules. Black square indicates the position of the close-up view shown in F. (F)
614 Wavy lamellar structure of the Birbeck granule. Black dots were gold nanoparticles used as
615 fiducial markers. (G) Class averages of the projection images of Birbeck granules. The image
616 dimension is 34 nm^2. Although 2D classification did not converge well due to the continuity

of the structure, some classes showed a porous structure with a honeycomb-like lattice.

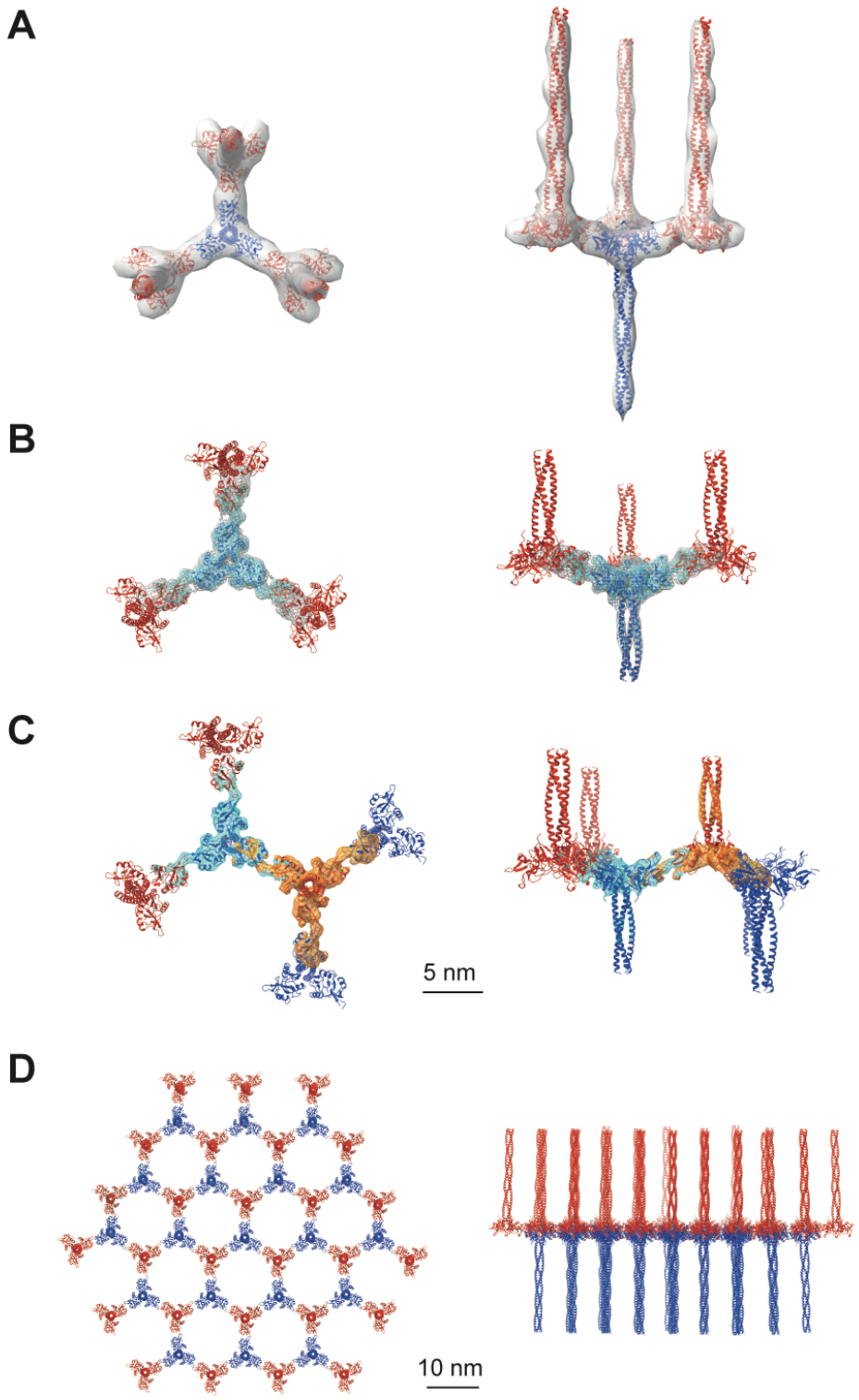

Figure 2

619

620 **Figure 2: Averaged subtomograms of Birbeck granules. (**A) Result of the initial 3D
621 refinement. The central langerin trimer (blue) binds to the three inverted langerin trimers
622 (red). (B) Result of the focused refinement. Improved resolution (6.4 Å) allowed secondary
623 structure modeling. The gray mesh and the cyan surface indicate low and high threshold
624 isosurfaces, respectively. (C) Result of the two-body refinement. The second body (orange)
625 was refined with respect to the first body (cyan). (D) Honeycomb model of the langerin lattice
626 within Birbeck granules. This honeycomb lattice is an ideal model, with the assumption of
627 structural uniformity. (A-D) left, top views; right, side views.
628
629

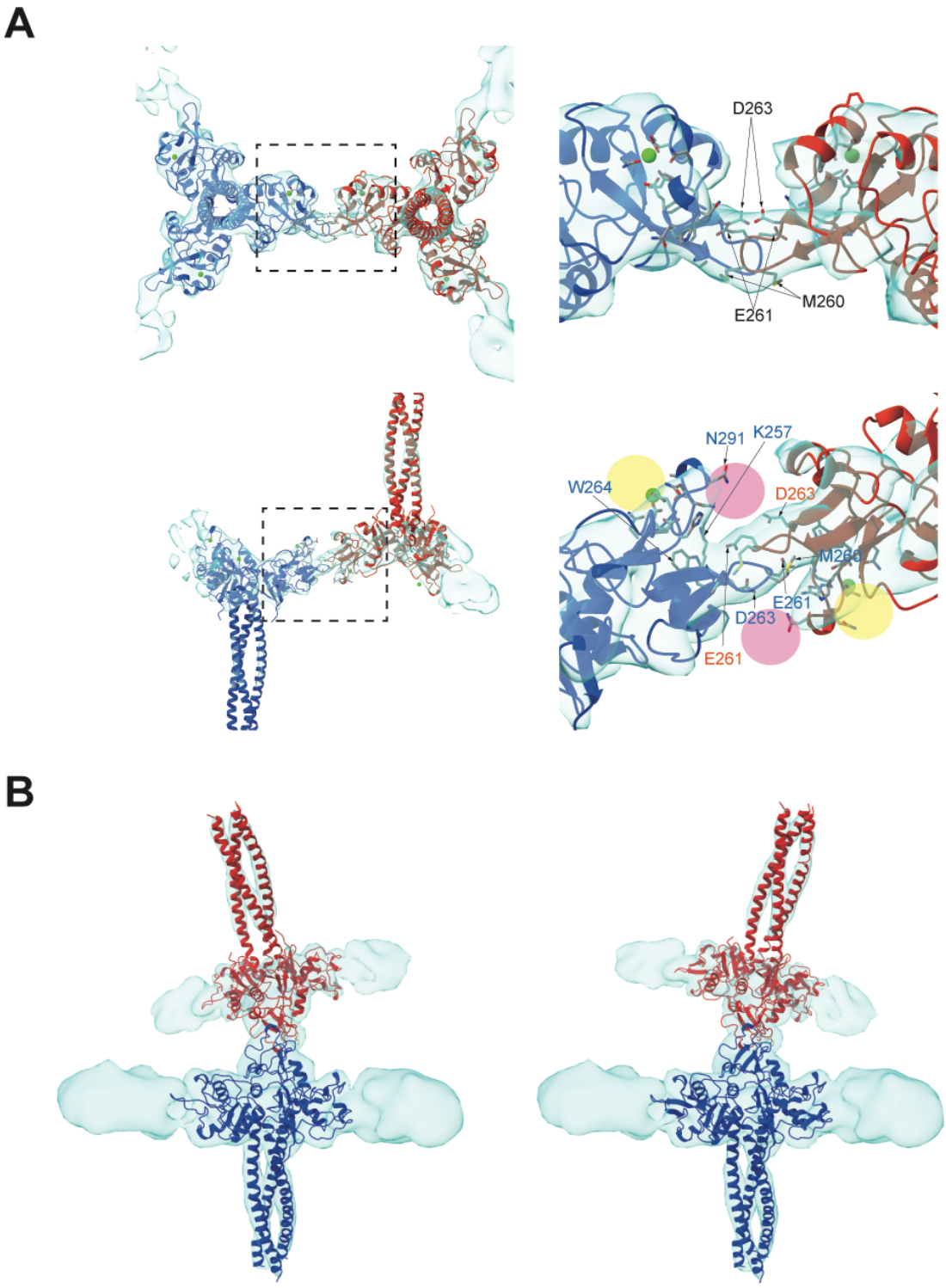

Figure 3

630

631 **Figure 3: Binding interface between two langerin trimers.** (A) Two langerin trimers
632 interact via the loops at residues 258-263. Amino acid codes and residue numbers are
633 indicated. Yellow and pink circles indicate the primary and secondary carbohydrate-binding
634 sites. The orientations of the side chains are speculative because the resolution of these maps
635 (6.4 Å) was insufficient for precise modeling. Calcium ions (green) were placed based on the
636 crystal structure (PDB ID: 3KQG). Top and side views are displayed in the top and bottom
637 rows, respectively. Broken squares indicate the positions of the magnified views on the right.
638 (B) Flexibility between the two trimers. The first eigenvector of the structural variation of
639 the inverted trimer (red) relative to the upright trimer (blue) shows an approximately 30°
640 rotation about the loop 258-263 (see Movie S2).
641
642

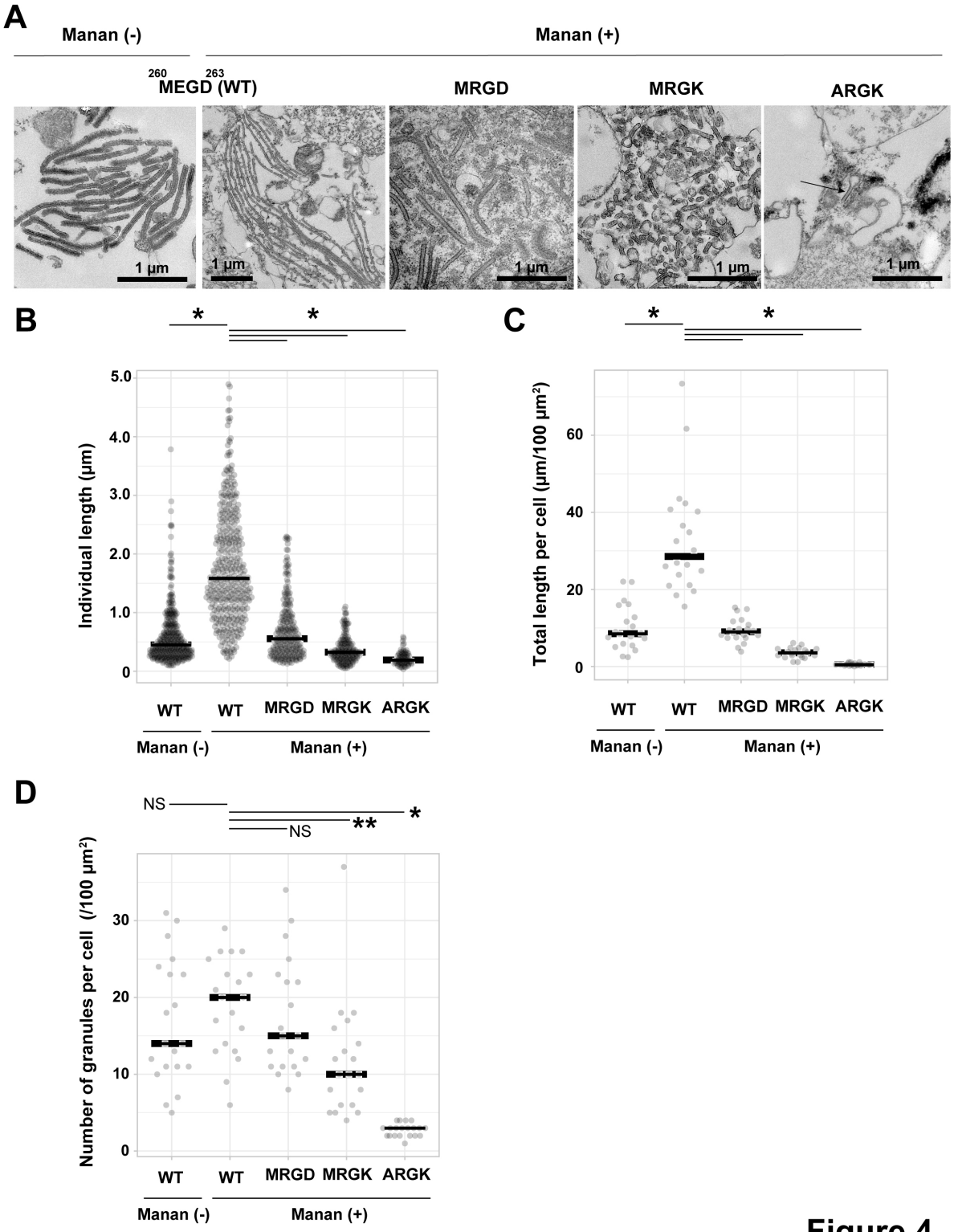
A
Manan (-)
Manan (+)
260 263
MEGD (WT)
MRGD
MRGK
ARGK
1 µm
B
Individual length (µm)
5.0
4.0
3.0
2.0
1.0
0
WT
WT
MRGD
MRGK
ARGK
Manan (-)
Manan (+)
C
Total length per cell (µm/100 µm²)
60
40
20
0
D
NS
NS
**
*
Number of granules per cell (/100 µm²)
30
20
10
0

Figure 4

644 **Figure 4: Mutations to the loop 258-263 disrupted Birbeck granule formation.** (A) Ultra-
645 thin electron microscopy of Birbeck granules with and without yeast mannan in langerin-
646 overexpressing 293T cells. Residues at 260-263 (Met-Glu-Gly-Asp, MEGD) were mutated
647 to Met-Arg-Gly-Asp (MRGD), Met-Arg-Gly-Lys (MRGK), or Ala-Arg-Gly-Lys (ARGK).
648 The Mannan (+) WT image has a lower magnification than the others in order to show the
649 entire Birbeck granules. (B-D) Quantification of Birbeck granule formation. Horizontal lines
650 indicate the median values. Single asterisks and the double asterisk indicate statistically
651 significant differences with $p < 0.01$ and $p = 0.0101$, respectively. NS indicates no statistically
652 significant differences. *p* values were calculated using Bonferroni-corrected Student's *t*-tests.
653 (B) Lengths of individual Birbeck granules were measured. N = 337 (WT mannan-), 386
654 (WT mannan+), 348 (MRGD), 233 (MRGK), and 70 (ARGK). (C) Sum of the length of
655 Birbeck granules per 100 μm^2 cell area. Cross-sections of cells with nuclei of > 5 μm in
656 diameter were selected and the total lengths of the Birbeck granules were measured within
657 the cells. N = 20 for all the samples. (D) Number of the Birbeck granules per 100 μm^2 cell
658 area. N = 20 for all the samples.
659
660

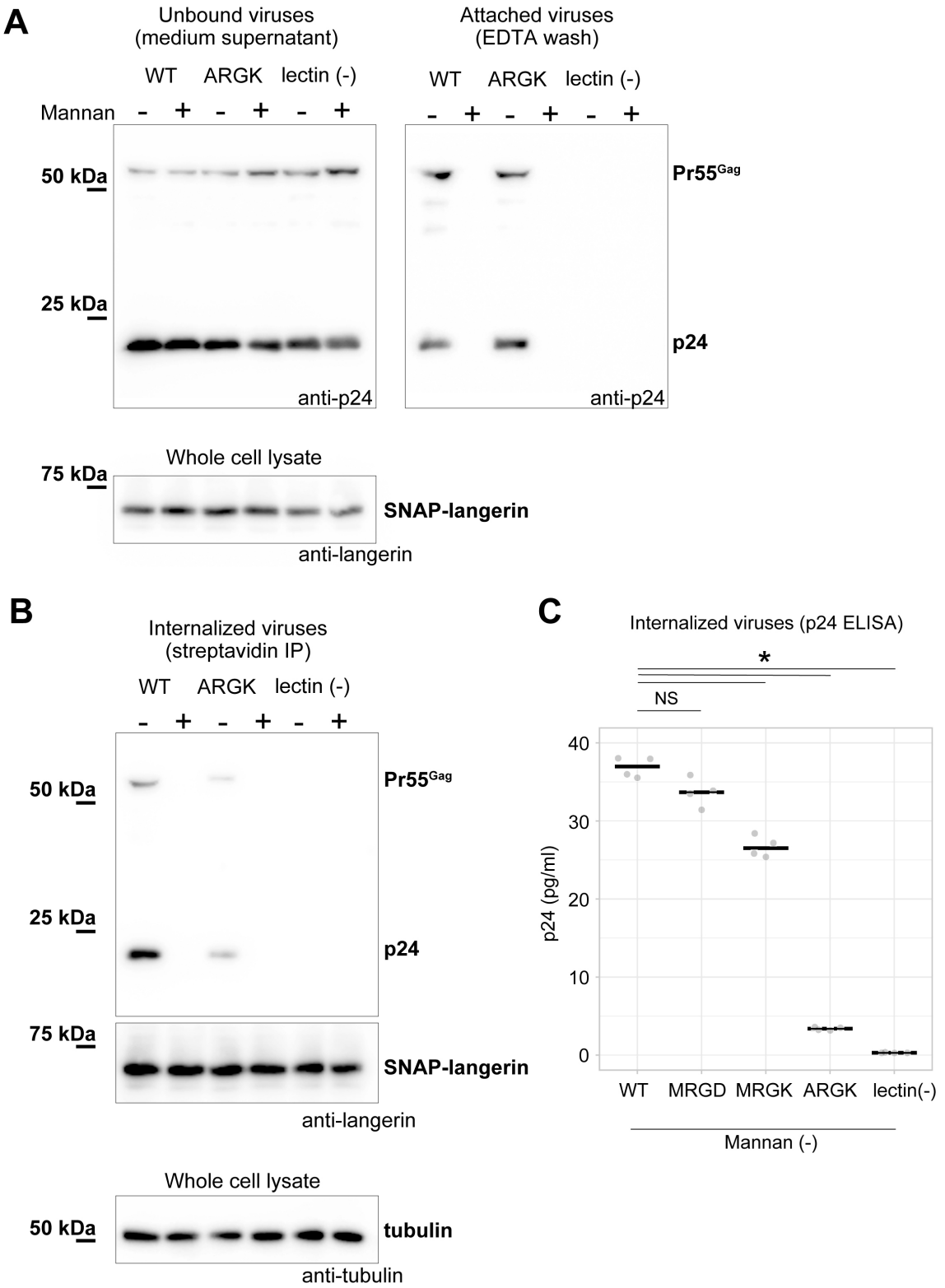
A
Unbound viruses
(medium supernatant)
Attached viruses
(EDTA wash)
WT ARGK lectin (-)
WT ARGK lectin (-)
Mannan - + - + - +
- + - + - +
50 kDa
25 kDa
Pr55Gag
p24
anti-p24
anti-p24
Whole cell lysate
75 kDa
SNAP-langerin
anti-langerin
B
Internalized viruses
(streptavidin IP)
WT ARGK lectin (-)
- + - + - +
50 kDa
25 kDa
75 kDa
Pr55Gag
p24
SNAP-langerin
anti-langerin
Whole cell lysate
50 kDa
tubulin
anti-tubulin
C
Internalized viruses (p24 ELISA)
*
NS
p24 (pg/ml)
40
30
20
10
0
WT MRGD MRGK ARGK lectin(-)
Mannan (-)

Figure 5

661

662 **Figure 5: Mutation to the loop 258-263 inhibited the internalization of pseudoviruses.**
663 HIV-1 pseudoviruses were added to langerin-expressing 293T cells. Yeast mannan (10
664 μg/ml) was added to block the lectin-dependent binding of pseudoviruses. A langerin mutant
665 lacking calcium binding ability (lectin (-)) was used as the negative control. (A) Immunoblots
666 of pseudoviruses attached to the cell surface. Unbound and attached viruses were collected
667 from the supernatant of the culture medium and TBS-EDTA buffer, respectively. Samples of
668 unbound viruses were diluted 50-fold to adjust the band intensities. The expression levels of
669 SNAP-tagged langerin show that the numbers of transfected cells were approximately the
670 same in each experiment. $Pr55^{gag}$ and p24 indicate unprocessed and fully-processed capsid
671 proteins, respectively. (B) Immunoblots of internalized pseudoviruses. Birbeck granules were
672 isolated by precipitation using streptavidin-agarose, and intracellular viruses and langerin
673 were detected by their respective antibodies. Tubulins in the whole-cell lysates were detected
674 for loading controls. (C) Quantification of internalized viruses using p24 ELISA. Horizontal
675 lines indicate the mean. NS and Asterisk indicate no significant difference and statistically
676 significant differences ($p < 0.001$) calculated using Bonferroni-corrected Student's *t*-tests
677 (N=4), respectively.
678

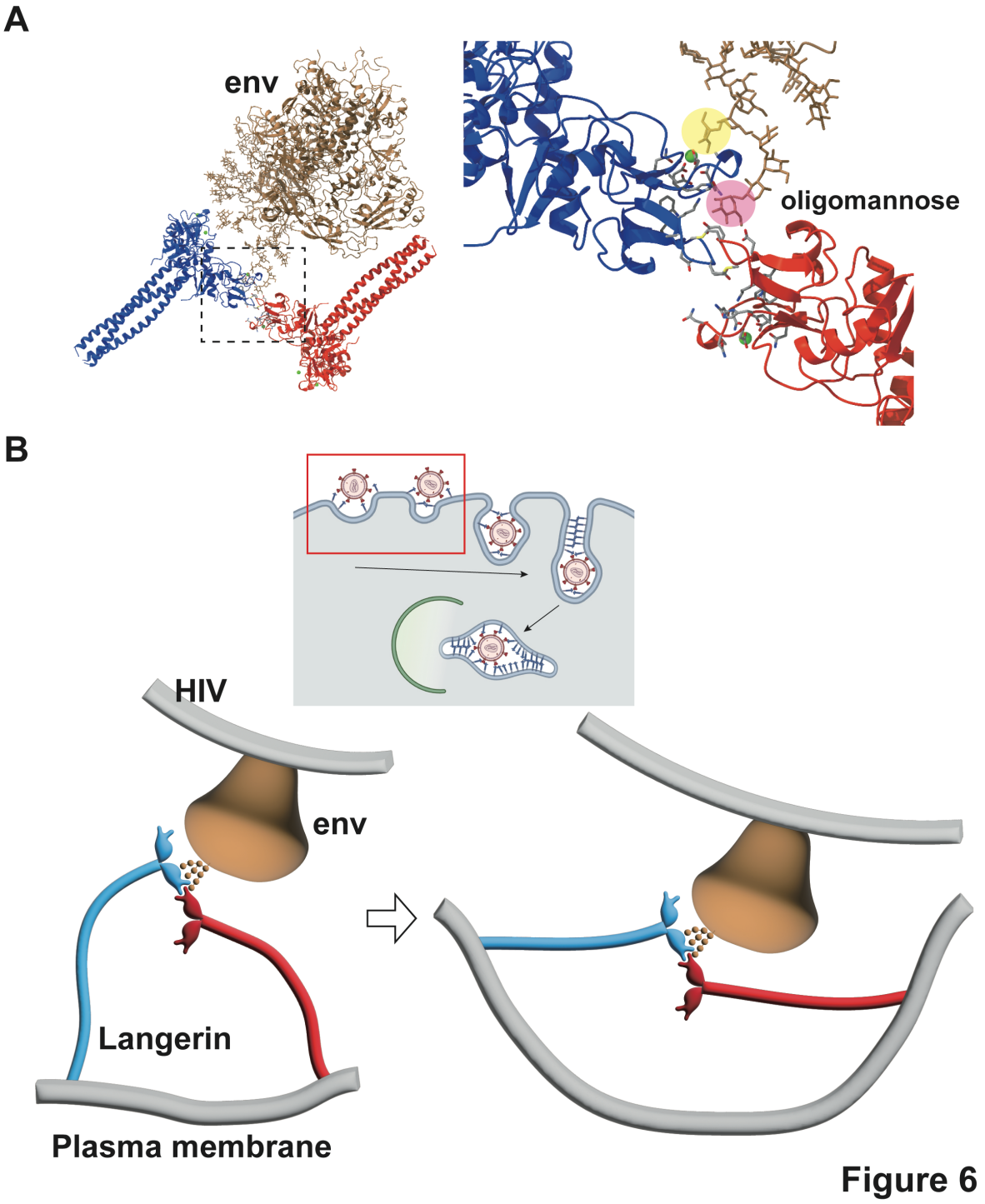

679

680 **Figure 6: Model of HIV internalization by langerin.** (A) Glycosylated structure of HIV-1

envelope (env, gray) (Constructed based on PDB ID: 5FYJ and 6ULC) bound to the langerin trimer complex. Branches of the high-mannose oligosaccharide interacting with the primary (yellow) and secondary (pink) carbohydrate-binding sites. The broken square indicates the position of the close-up view on the right. (B) Schematics of HIV internalization by langerin. The inset on the top shows an overview of antigen processing within a Langerhans cell. Viruses are captured by langerin, internalized into a Birbeck granule, and degraded by the autophagic system. The red square indicates the viral entry process described in the lower panels. The high-mannose oligosaccharide on HIV-1 env first binds to the primary carbohydrate-binding site, and one of the branches of the oligo-mannose weakly interacts with the secondary binding site. The flexible neck region allows docking of the loop 258-263 of an adjacent trimer into the secondary carbohydrate-binding cleft, reinforcing the binding of the oligo-mannose. As the elastic neck regions straighten, the plasma membrane is deformed into a lamellar invagination, which internalizes the virus.

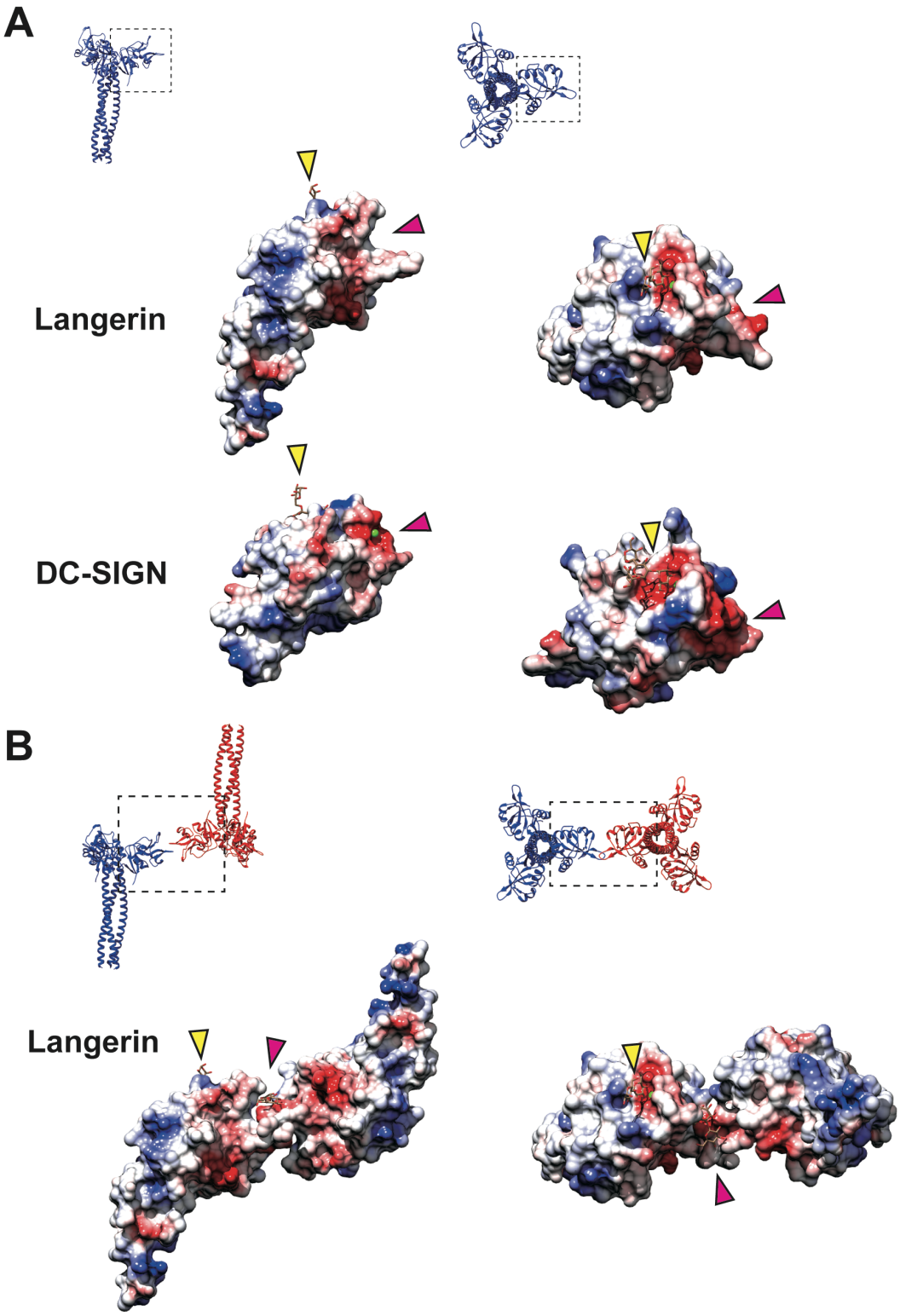

Figure 7

696

697 **Figure 7: Coulombic surfaces of the carbohydrate-binding sites.** (A) Comparison of the
698 surface charge between the CRDs of langerin and DC-SIGN (PDB ID: 1SL4). Blue and red
699 coloring indicates positive and negative charges, respectively. The primary and secondary
700 carbohydrate-binding sites are indicated by yellow and pink arrowheads, respectively. The
701 region of DC-SIGN corresponding to the secondary carbohydrate-binding sites of langerin is
702 occupied by calcium ions (green) and does not form a cleft. (B) Surface model of the langerin
703 trimer complex. Mannose ligands are placed based on a previously proposed model (Chatwell
704 et al., 2008). (A-B) Broken squares indicate the position and the orientation of the side (left)
705 and the top (right) views. Oligosaccharide ligands are shown in gray.
706
707